

OPEN ACCESS

Accelerated Iridium Dissolution in Proton Exchange Membrane (PEM) Water Electrolyzers by Inert Mobile Anions Adsorbed in the Double Layer

To cite this article: Maximilian Schalenbach et al 2025 J. Electrochem. Soc. 172 064509

View the article online for updates and enhancements.

You may also like

- Gas Crossover in Membrane Electrolyzers—The Impact of MEA Conditioning on Gas Permeability Leander Treutlein, Ali Javed, Niklas L.
- Tuning Interfacial Water Structural Entropy to Promote pH-Dependent HOR/HER Activity on Pt

Nicholas J. Oliveira and Yushan Yan

- Design and Characterization of Gel Polymer Electrolytes Incorporating Highly Concentrated Electrolytes: Impact of Solidification on Bulk and Electrochemical

Rintaro Mogi, Reita Furui, Koji Hiraoka et

ECC-Opto-10 Optical Battery Test Cell: Visualize the Processes Inside Your Battery!



- ✓ Battery Test Cell for Optical Characterization Designed for light microscopy, Raman spectroscopy and XRD.
- ✓ Optimized, Low Profile Cell Design (Device Height 21.5 mm) Low cell height for high compatibility, fits on standard samples stages.
- ✓ High Cycling Stability and Easy Handling Dedicated sample holders for different electrode arrangements included!
- Cell Lids with Different Openings and Window Materials Available





Contact us:

- +49 40 79012-734
- sales@el-cell.com
- www.el-cell.com









Accelerated Iridium Dissolution in Proton Exchange Membrane (PEM) Water Electrolyzers by Inert Mobile Anions Adsorbed in the Double Layer

Maximilian Schalenbach, ^{1,z} Niklas Wolf, ^{1,2} Jean-Pierre Poc, ^{1,2} Christine Heume, ^{1,2} Shibabrata Basak, ¹ Roland Schierholz, ¹ Andre Karl, ¹ Eva Jodat, ¹ and Rüdiger-A. Eichel ^{1,2}

Iridium oxides display state-of-the-art electrocatalysts for anodes in proton exchange membrane water electrolyzers (PEM-WE), combining electrocatalytic activity for the oxygen evolution reaction (OER) and reasonable stability. During OER with liquid electrolytes, iridium dissolution rates were reported as orders of magnitude higher than those of operating PEM-WE cells, while the reasons for these differences are not well understood. Here, iridium oxide dissolution in an operating PEM-WE cell is examined with different feeds, including pure water, 0.1 M sulfuric acid, and 0.1 M perchloric acid. With sulfuric acid feed, the electrically contacted iridium oxide at the anode is found to dissolve within 22 h. In comparison, the dissolution rates with perchloric acid addition and pure water are approximately 120 and 1500 times smaller, respectively. These differences are explained with a novel theory that correlates the influence of inert mobile anions on dissolution rates by their adsorption in the electrochemical double layer. This physicochemical effect also explains previously reported discrepancies of reported iridium dissolution rates with different electrolytes. Based on the results, the quality of the feed water in terms of inert anion pollution is highlighted as a critical factor for achieving long life of PEM-WE cells with low iridium loadings.

© 2025 The Author(s). Published on behalf of The Electrochemical Society by IOP Publishing Limited. This is an open access article distributed under the terms of the Creative Commons Attribution 4.0 License (CC BY, https://creativecommons.org/licenses/by/4.0/), which permits unrestricted reuse of the work in any medium, provided the original work is properly cited. [DOI: 10.1149/1945-7111/ade0ef]

Manuscript submitted December 3, 2024; revised manuscript received June 3, 2025. Published June 13, 2025. This paper is part of the JES Focus Issue on Proton Exchange Membrane Fuel Cell and Proton Exchange Membrane Water Electrolyzer Durability III.

In the late 1960s, the development of electrolyzers operating with proton exchange membrane (PEMs, often also referring to as polymer electrolyte membranes) started. Similar to today's stateof-the-art, these early works used perfluorosulfonic acid (PFSA)² based PEMs in combination with iridium oxide catalysts at the anode³⁻⁵ (the oxygen electrode) and carbon supported platinumnanoparticles at the cathode⁶ (the hydrogen electrode). In 1973 remarkable voltage-current-characteristics of PEM-electrolyzers were reported, with similar components of that of today's devices. Fridium oxides combine activity and stability for the oxygen evolution reaction, displaying the most suitable electrocatalysts for the OER in acidic media. Unlike the weakly conducting or insulating oxides of most transition metals, the rutile phase of iridium oxide shows the conductivity of a metal⁸ that originates from a conduction band in the electronic structure. This outstanding conductivity facilitates the fabrication of electron-conducting catalysts layers, which typically consist of mixtures of iridium particles and PFSA ionomer binder.

A drawback of iridium-based anodes is the element's scarcity as it displays one of the least abundant non-radioactive transition metal in the earth's crust. ¹¹ Moreover, the electrochemical dissolution during the OER ^{12–14} may display a bottleneck for reducing iridium contents in PEM electrolyzers. ^{15,16} Pourbaix ¹⁷ described in his monumental "atlas of electrochemical equilibria" thermodynamically stable states of metals in aqueous media as a function of the pH and potential. In the recent literature, the electrode potentials for the corrosion processes stated by Pourbaix were shown to precisely relate to measured dissolution of noble metals, ¹⁸ proving the accuracy of his work. Besides the Ir³⁺ cation as dissolution product, Pourbaix's also stated a [IrO₄]²⁻ complex as possible dissolution outcome. Nowadays, the iridium dissolution products are still not clarified. ¹⁹ With modern thermodynamic computations, the surface energies of IrO₂ can be calculated as a function of the surface orientation and related to the electrode potentials, ²⁰ giving more

insights to the stability from a thermodynamic point of view than the classical bulk-related data of Pourbaix.

The +4 oxidation state of iridium in the rutile oxide is reported to change between +3 to +6 during the OER²¹⁻²⁴ as a result of intermediate reaction states. These changing oxidation states and the role of oxygen from the lattice lead to dynamic recrystallization of the oxide during the OER. ^{13,25–28} Such recrystallization processes are known to result in severe corrosion^{7,29} and are at least partly responsible for the dissolution of iridium oxide during the OER. 30,31 These dynamic processes of switching oxide states and recrystallizations of the lattice as well as the accompanied lattice-strain are not incorporated in the thermodynamic considerations of equilibrated states from Pourbaix's work, ¹⁷ in which the rutile phase of iridium oxide has been considered as thermodynamically stable in the typical operating regime of a PEM electrolyzer. The complexity of the iridium dissolution process (including the above described effects) is currently not portrayable by quantum mechanical models and therefore the understanding of the dissolution process relies on experimental works. However, due to a lack of resolution, the dissolution process of single atoms or ions is currently not experimentally resolvable. Macroscopic measurements 14,31,32 display the only reliable source of information to characterize the factors that affect the physicochemical process of the iridium dissolution during the OER.

The limited availability of iridium and the worldwide production of only about 6 tons per year require low iridium loadings^{33–36} to meet the future global demand for renewable hydrogen with the PEM-WE technology. ^{16,37} An operating PEM-WE cell with a low iridium loading of 80 μg cm⁻² showed severe iridium dissolution within just a few thousand hours of operation. ¹⁵ To better characterize the iridium dissolution during the OER, the stability number, defined as ratio of produced oxygen molecules to dissolved iridium atoms, was introduced. ³¹ Studies have thoroughly examined the stability number of iridium based OER catalysts in aqueous electrolytes, correlating these values (ranging from 10⁴ to 10⁷) with catalyst structure and preparation methods. ^{14,31,32} Notably, iridium dissolution rates observed in aqueous electrolytes during the OER are higher than those in PEM electrolyzers, albeit the

¹Institute of Energy Technologies (IET-1): Fundamental Electrochemistry, Forschungszentrum Jülich, 52425 Jülich, Germany

²Institute of Physical Chemistry, RWTH Aachen University, 52056 Aachen, Germany

Table I. Overview of the experiments with the PEM-WE cell.

Name experiment	Anodic IrO ₂	Feed	Duration @ 1 A cm ⁻²
H ₂ O	Yes	Pure H ₂ O	145 h
H_2SO_4	Yes	$0.1 \text{ M H}_2\text{SO}_4$	22 h
HClO ₄	Yes	0.1 M HClO ₄	145 h
H ₂ SO ₄ , no Ir	No	$0.1 \text{ M H}_2\text{SO}_4$	22 h
HClO ₄ , no Ir	No	0.1 M HClO ₄	22 h

physicochemical reasons for this discrepancy are unresolved. 32,38,39 For instance, comparing the dissolution data of Yu et al. 15 and Eheleben et al. 39 reveals a more than ten times longer lifetime of the iridium catalyst in a PEM-WE cell at 80 °C than that observed in less acidic aqueous solutions at room temperature. Understanding the underlying physicochemical mechanisms for such observations display the main motivation for this work.

In this study, the iridium dissolution of an operating PEM-WE cell is investigated with the intentional addition of sulfuric acid and perchloric acid to the cell's water supply. Thus, the effect of inert sulfate and perchlorate anions on the physicochemical mechanisms of anodic iridium dissolution are examined. In industrial application, the major anion impurity of the supply water is typically chloride, for which the iridium degradation has been thoroughly examined in the literature. ^{40–43} By electro-oxidation to chlorine, chloride impurities can be decomposed, for which the related iridium dissolution displays a fundamentally different corrosion mechanism than that in the case of the inert ions. To enable acid addition to the feed water, a PEM-WE cell with a corrosion-resistant design is developed. By using acid concentrations of 0.1 M in the water supply, the proton concentration of 2.7 M in the water channels of fully hydrated Nafion (the most prominent PFSA material for fuel cells and electrolyzers)⁴⁴ is only slightly changed. However, the introduced mobile anions are found to drastically increase the iridium dissolution. Six hypotheses are presented that aim to explain the influence of mobile ions on the iridium dissolution. Among these hypotheses, the effect of mobile anions on the spatial charge distribution in the electrochemical double layer at the iridium oxide catalysts displays the most suitable explanation to describe the different impacts of sulfates and perchlorates on the dissolution. This novel theory brings together corrosion and double layer adsorption as thus far rather uncorrelated fields in electrochemistry. This interpretation shines light from a new angle onto a long-lasting literature debate^{32,45} about the discrepancy of iridium dissolution in liquid and polymer electrolytes during the OER. Moreover, these findings highlight that the water quality plays a decisive role for the stability of iridium catalysts for the OER in PEM electrolyzers.

Methods

Water electrolysis measurements.—A PEM-WE cell is typically constructed with a porous titanium-based material as anodic current collector, a titanium anodic flow field, porous graphite fleece as the cathodic current collector, and a graphite flow field for the cathode.⁶ If acids are added to this cell assembly, the titanium-based anodic materials will show severe dissolution and passivation that causes contact resistances. To make the cell assembly resistant to such corrosion, a platinum coating of the anodic flow field (flow fields made in house, 46 platinum coating by Metakem) protected the titanium base material, while two stacked platinum meshes served as the anodic current collector. The platinum mesh facing the membrane was a 100-mesh woven from 0.0762 mm wire (Thermo Scientific), which was mechanically supported by an underlying 52mesh woven from 0.1 mm wire (Thermo Scientific). Before the cell was assembled, the platinum meshes were treated in an open flame to burn residuals of previous measurements. Three stacked carbon papers (Toray TGP-H60) were used as the cathodic current collector. PTFE flat sealings with thicknesses of 625 µm and 350 µm

(Westring Dichtungstechnik GmbH) were employed for anode and cathode, respectively.

Table I summarizes the five experimental setups used in this study, with different membrane electrode assemblies (MEAs) and feed water supplies. Three of the five experiments were conducted using MEAs with both anodic and cathodic catalyst layers. In the remaining two experiments, single-sided MEAs were used, which were equipped with a platinum-containing cathode catalyst layer but without an anodic catalyst layer. This configuration serves as a reference to benchmark the voltage-current (UI) characteristic of the cell without anodic iridium catalyst. All MEAs (HYDRionTM N115) were purchased from Ion Power GmbH and were based on a Nafion N115 Membrane. The manufacturer's data sheets of the catalyst layers reported an anodic iridium content of 1 mg cm⁻² and a cathodic platinum content of 0.3 mg cm⁻². The manufacturer's batch number for the anode and cathode coated membranes was 5072, while it was 4313 for the membranes with cathode but without anode coating. Two feeds of 0.51 each were pumped along the anode and cathode-side with flow rates of 20 ml min⁻¹, respectively. To compensate for the water drag of the proton transport through the membrane, 47,48 a pump continuously carried the liquid excess from the cathodic gas separator to that of the anode. The cell was operated at atmospheric pressure and heated to 60°C.

The measurement procedure to characterize these MEAs included: (i) Conditioning the cell at 1 A cm⁻² for one hour. (ii) Measurement of the voltage-current (UI) characteristic. (iii) Constant current density of 1 A cm⁻² for 22 h or 145 h. (iv) Measurement of the UI characteristic. The current-voltage (UI) characteristics were measured using a VMP-300 potentiostat from BioLogic Science Instruments Ltd in galvanostatic mode. Different current steps were applied, each maintained for 60 s to obtain steady-state conditions. The voltage at each current step was determined by calculating by averaging the recorded values of the last 20 s of the total 60 s interval.

Microscopy.—After the electrochemical measurements, the MEA used in the experiment with the 0.1 M sulfuric acid feed was analyzed with scanning electron microscopy (SEM) and energy dispersive X-ray spectroscopy (EDS) to determine the elemental composition of the anodic and cathodic catalyst layer, respectively. A xenon plasma focused ion beam scanning electron microscope (TESCAN Amber X; TESCAN) was used for imaging and cross-sectional sample preparation. Samples cut from a larger membrane into 1×1 cm pieces were mounted on SEM stubs with carbon tape. Secondary electron (SE) imaging was performed using the integrated Everhart-Thornley (E-T) detector, together with low energy back-scatter electron (LE BSE) imaging for compositional contrast. Imaging parameters included a dwell time of 3 μs, an imaging current of 300 pA, and an accelerating voltage of 2 keV. Tilt correction was applied for cross-sectional imaging.

Cross-sectional focus ion beam (FIB) milling was performed at a working distance of approximately 6 mm, with the electron and ion beams aligned at the point of intersection and the sample tilted at 55°. The xenon plasma FIB was initially operated at 30 kV and 50 nA for rough milling, with the energy progressively reduced for finer milling steps, reaching 1 nA for the final polishing step. This process resulted in a final cross-sectional width of $100\,\mu m$. Compositional analysis by EDS was conducted with an "EDAX

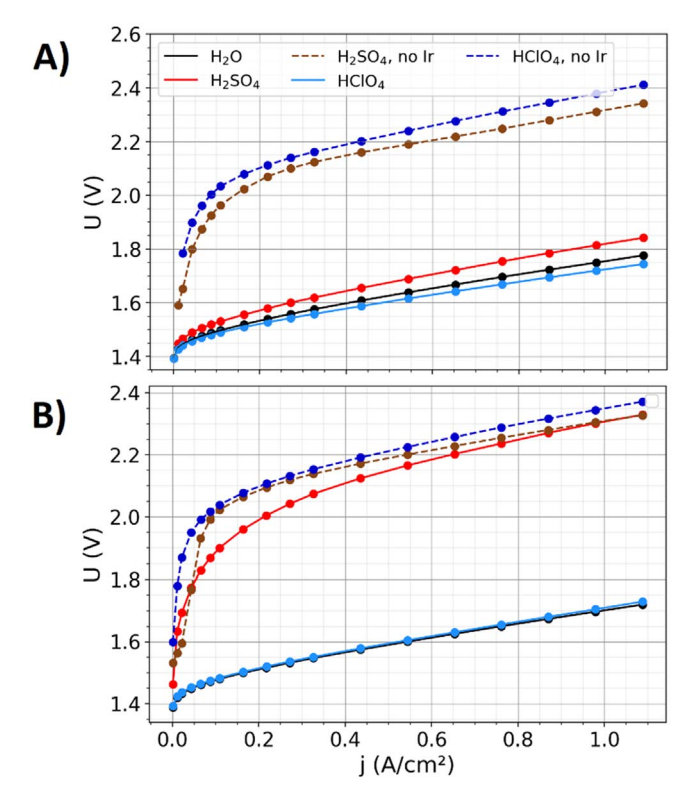


Figure 1. Voltage-current (UI) characteristics of the different configurations of the electrolysis cell at an operating temperature of 60 °C. Colors: Different feed supplies and MEA types. (A) Initial UI characteristics. (B) Final UI-characteristic after operating the cell at a current density of 1 A cm⁻² for the times stated in Table I.

Elite Super detector" and "EDAX Apex Advanced" software for data acquisition and analysis. The EDS parameters varied according to the sample area: an acceleration voltage of 5 keV and a beam current of 300 pA were used for the analyses of the anodes and its cross-sections, while 30 keV and 1 nA were used for the investigations of the cathode side.

Electrolyte analytics.—An Agilent 7900 inductively coupled plasma mass spectrometer (ICP-MS) was used to analyze the feed water for iridium. Three measurements of each feed water were conducted, while their standard deviation served as measure for the error

Results and Discussion

Electrochemical data.—Figure 1A shows the voltage-current (UI) characteristics of the different cell setups that are summarized in Table I. Independent of the feed used, the MEAs equipped with anodic and cathodic catalyst layer initially all show UI-characteristics that correspond to the typical state-of-the-art performance at such temperature and membrane thickness.⁴⁹ Within a window of ±50 mV, these voltage-current characteristics are equal. Mobile anions introduced with the feed water are reported to affect the catalytic properties. 50,51 Fully hydrated Nafion has an intrinsic proton concentration of approximately 2.7 M in the water channels,⁴⁴ which is supplied by the sulfonic acid functional groups. By adding acids with concentrations of 0.1 M to the water supply, the proton concentration in the aqueous phase of Nafion increases by approximately 7.4% and 3.7% for sulfuric acid and perchloric acid, respectively. Hence, the pH inside the membrane remains mostly unchanged. Iridium dissolution mechanisms are reported to alter with significant pH changes between the acidic and alkaline regime.⁵² However, the negligible influence of the added acids on the pH cannot substantially alter the mechanisms of the iridium dissolution. Besides such physicochemical influences of the changed feed water on the cell performance, variations in the MEA manufacturing and cell assembly typically lead for differences of the voltage-current characteristics within the same order of magnitude as the observed ±50 mV. At current densities above 0.1 A cm⁻², the setups with the anodic catalyst layer show approximately 0.6 V lower cell voltages than those without the anodic catalysts, where the OER takes place at the anodic platinum current collector.

Figure 1B shows UI-characteristics after conducting the measurements in Fig. 1A and an additional operation of 22 h or 145 h (see Table I) at 1 A cm⁻². The UI-characteristics of the two-sided MEAs with water and perchloric acid are similar to those initially recorded. In contrast, the two-sided MEA operated with sulfuric acid feed showed a drastic degradation with a similar UI-characteristic to that of the MEAs without an anodic catalyst layer.

Figure 2A shows the cell voltage of the different cell modifications at a constant current density of 1 A cm⁻² over time, which was obtained between the measurements presented in Figs. 1A and 1B (see protocol in the Methods section). With pure water and 0.1 M perchloric acid supply, the cell voltage increases by less than 0.05 V within 145 h of operation. With 0.1 M sulfuric acid feed, the cell voltage drastically increases from approximately 1.85 V to approximately 2.4 V within only 17 h of operation. A similar cell voltage is obtained for the setups without anodic catalyst layers, in which the anodic platinum current collector serves as OER catalyst. Hence, the voltage increase over time in Fig. 2A with 0.1 M sulfuric acid feed is associated with a loss of the electrically contacted anodic iridium.

Table II shows the iridium loss of the experiments with the twosided MEAs as measured by inductively coupled plasma mass spectrometry (ICP-MS) of the feed after the electrochemical measurements. Figure 2B shows the iridium losses of Table II normalized to the cell area. After 145 h of operation with initially pure water, approximately $0.4 \, \mu \mathrm{g \ cm^{-2}}$ iridium is measured in the feed. By operating the cell with 0.1 M perchloric acid, approximately 5 µg cm⁻² iridium is measured in the feed. In the case of 0.1 M sulfuric acid feed, approximately $95 \,\mu \mathrm{g \, cm^{-2}}$ iridium is measured after an operation of just 22 h, which corresponds to approximately 10% of the initial anodic iridium loading. Normalizing these measured concentrations to the operation time, a dissolution rate of approximately 3, 34, and 4323 ng cm⁻² result for the operation with pure water, 0.1 M perchloric acid, and 0.1 M sulfuric acid feed, respectively. However, these dissolution rates do not include the iridium electrodeposited at the cathode, which is examined below in more detail. Besides iridium, the water feed was also tested for platinum, titanium, and iron. Titanium and iron were close or below the detection limit for all measurements. The platinum contents follow a similar trend as that of iridium, which is expected to originate from the anodic platinum used as current collector and flow field coating. The following discussion for the iridium dissolution is also applicable for the mechanisms of the anodic platinum dissolution.

Analysis of the MEA operated with H_2SO_4 feed.—In the following, a scanning electron microscopy (SEM) and energy dispersive X-ray spectroscopy (EDS) analysis of the MEA with iridium catalyst after the operation with H_2SO_4 feed is presented. Figure 3A shows a SEM image of the cathode, while Figs. 3B and 3C show EDS elemental maps of iridium and platinum of the same frame, respectively. The EDS elemental composition analysis indicates a platinum to iridium ratio of 10. Hence, in addition to the dissolved iridium graphed in Fig. 2B, iridium is also deposited at the cathode, which agrees with previous reported long-term examinations of the iridium dissolution in PEM-WE cells. The deposited iridium can originate from the amount dissolved in the feed water or from ions coming directly from the anode through the membrane.

Figure 3D shows a top-view SEM image of the anode side of the MEA. The platinum mesh was pressed onto the anode side of the MEA, leaving spots with imprints of a compressed catalysts layer.

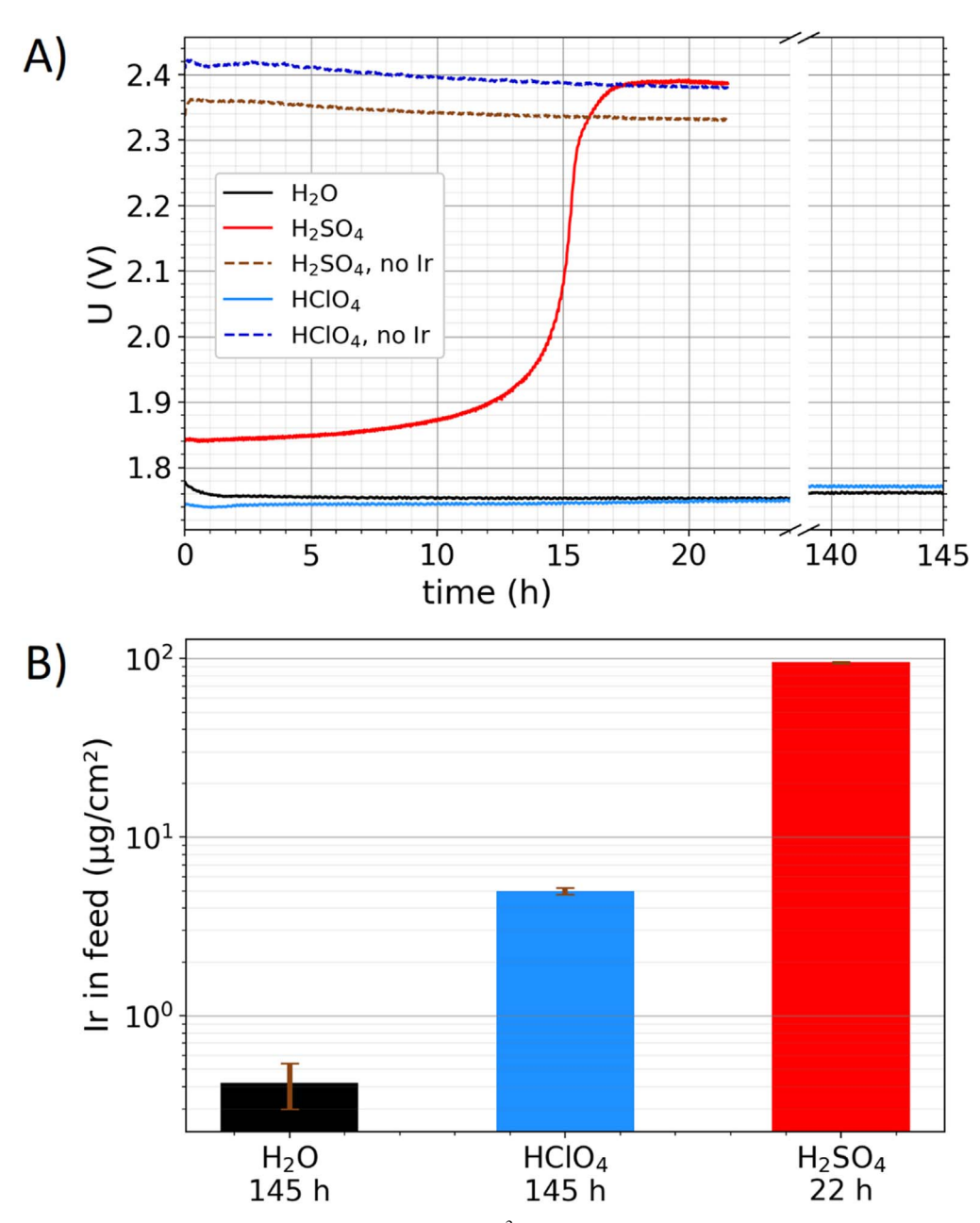


Figure 2. (A) Time evolution of the cell voltage at a current density of 1 A cm⁻² for the different MEAs and feeds used with the PEM-WE cell. (B) Dissolved iridium (measured by inductively coupled plasma mass spectroscopy) in the feed normalized to the cell area (only experiments with iridium containing MEAs, see Table I). The feeds were analyzed after the measurement protocol described in the Methods section was completed.

Table II. Results of the ICP-MS analysis of the feed after the experiment shown in Fig. 2A. The comparators "<" indicate that within the detection limit not any contamination could be measured. The other values correspond to average and standard variation of three individual measurements of the analyzed solution.

Feed	Duration	Ti $[\mu g l^{-1}]$	Fe [μg l ⁻¹]	Ir [μ g l ⁻¹]	P t[μ g l ⁻¹]
H ₂ O	145 h	<20	<30	0.42 ± 0.12	<0,2
$HClO_4$	145 h	22 ± 7	<30	4.99 ± 0.19	0.79 ± 0.09
H_2SO_4	22 h	34 ± 4	42 ± 7	95.1 ± 1.2	34.5 ± 0.9

Due to this compression, the catalyst layer is locally compacted at the contact areas with the platinum mesh. The topology of the surface leads to shadows in the SEM image, in which the deeper lying parts are partly weakly illuminated due to the incidence angle of the electron source. These shadows complicate an elemental EDS analysis, for which cross-sections are made to get a clear view on the elemental distribution in the catalyst layer. Figure 3E shows a SEM image with two trenches cut into the MEA that were prepared by using a focused ion beam (FIB). One of the trenches is prepared within the area of an imprint, while the other is outside the imprint.

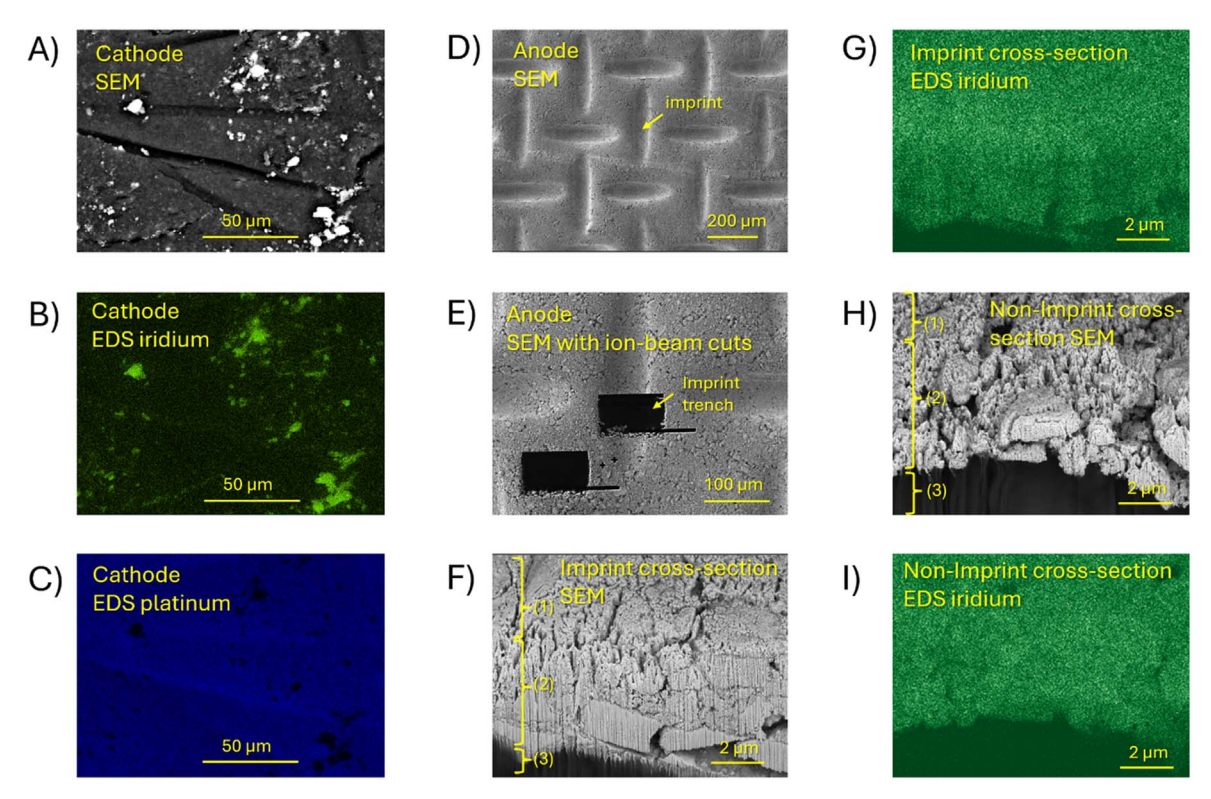


Figure 3. SEM and EDS images of the MEA with iridium catalyst after the operation with 0.1 M sulfuric acid feed. (A) SEM image of the cathode. (B) EDS elemental map of iridium at the cathode. (C) EDS elemental map of platinum at the cathode. (D) SEM image of the anode. (E) SEM picture with ion beam cuts in the imprint and outside the imprints that are left from the current collector. (F) Tilted view (55°) of the cross-section at the ion-beam cut within in the imprint of the current collector. The image shows a top view of the catalyst layer (1), the cross-section of the catalyst layer (2), and the membrane (3). (G) Elemental map of iridium at the cross-section within the imprint. (H) Tilted view (55°) of the cross-section at the ion-beam cut outside in the imprint of the current collector. Same notation of the numbers as those in (F). (I) Elemental map of iridium at the cross-section outside the imprint.

Figure 3F shows a SEM image of the cross-section inside the trench of the imprint, providing a clear view on the catalyst layer. Figure 3G shows the elemental map of the iridium distribution from this area. Iridium is still present in and on top of the imprint, even though the electrochemical measurements with the sulfuric acid feed in Figs. 1B and 2A did not indicate any catalytic effect of iridium after 22 h of operation. When the iridium catalyst dissolves, the Nafion binder of the composite electrode remains and forms a Nafion film on the left iridium. This film inhibits the electrical contact of the iridium catalyst, preventing it from contributing to the electrochemical OER. However, this film cannot be observed with EDS, as the penetration depth of the electrons⁵³ that excite the X-ray emission for the EDS analysis is larger than the presumably less than micrometer thick Nafion film on the iridium catalyst. As a result, the EDS analysis of Fig. 3G shows iridium on top of the catalysts layer in the imprint-area, despite it is presumably covered by a thin Nafion film. For comparison, Fig. 3H shows an SEM image and Fig. 3I the associated elemental iridium map at the crosssection of the non-imprint area of the MEA with SEM. Nafion film coverage as the origin of the lost iridium activity in Figs. 1B and 2A cannot be experimentally proven. An alternative interpretation of the presented cell voltage increase during the operation with 0.1 M sufuric acid feed is deactivation by poisoning, which however is not in line with the observed iridium dissolution rates in Fig. 2B. Hence, Nafion film coverage on remaining iridium displays the most reasonable interpretation to explain all the observed experimental data.

Discussion on the mechanisms of the iridium dissolution.—As discussed in the Introduction, the +4 oxidation state of iridium is reported to change between +3 to +6 during the OER $^{21-24}$ as a result of intermediate reaction states. The resulting dynamic recrystallization of the surface $^{13.25-28}$ during the OER is not well understood, leading to unknown starting points for the dissolution process. Hence, these restrictions of the current knowledge limit the

following discussion on the dissolution processes. To explain the influence of the added acids on the measured iridium dissolution rates, first the chemical pathways for the dissolution will be discussed. Second, the influence of acid anions on the electrochemical interface will be elucidated. Third, six hypotheses to explain the measured iridium dissolution as a function of the different feeds will be thoroughly elucidated.

Chemical dissolution pathways.—Kasian et al. ¹⁹ discussed chemical dissolution pathways for iridium oxide, including the dissolution of iridium as cations from an HIrO₂ intermediate state during the oxygen evolution

$$HIrO_2 + 3H^+ \rightarrow Ir^{3+} + 2H_2O,$$
 [1]

and the dissolution as anion complexes $[IrO_4]^{2-}$ from another intermediate state IrO_3 :

$$IrO_3 + H_2O \rightarrow [IrO_4]^{2-} + 2H^+.$$
 [2]

In Eq. 1, all oxygen atoms are removed during the dissolution process, forming a cation with the oxidation state of +3. An electrochemical transformation of IrO_2 to dissolved Ir^{3+} may also be possible:

$$IrO_2 + 2H_2O \rightarrow Ir^{3+} + 2O_2 + 4H^+ + 7e^-.$$
 [3]

Similarly, $[IrO_4]^{2-}$ may be formed with an electrochemical reaction from IrO_2 :

$$IrO_2 + 2H_2O \rightarrow [IrO_4]^{2-} + 4H^+ + 2e^-$$
 [4]

The Nernst potentials of the dissolution mechanisms are disputable, ⁵² as experimental thermodynamic data on the dissolution

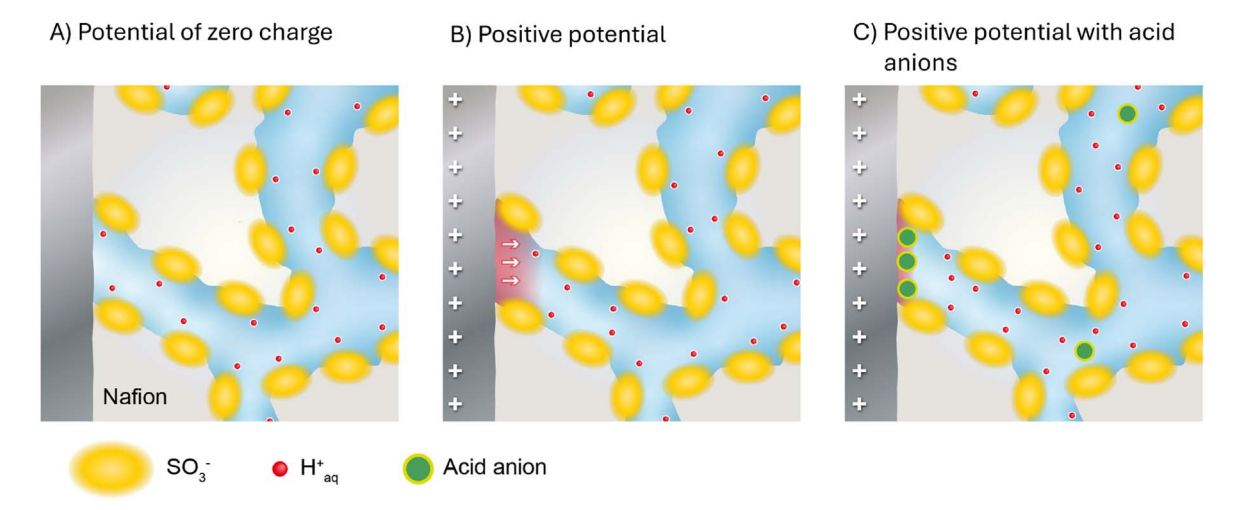


Figure 4. Schematic sketches showing the electrochemical interface between the electrode (dark grey) and Nafion with the aqueous phase (blueish) and polymeric phase (light greyish). Red Dots: Protons. Yellow dots: Immobile sulfonic acid groups of Nafion. Green dots: Mobile inert anions. (A) Interface at the potential of zero charge without mobile anions. (B) Charged electrode-Nafion interface without mobile ions, leading to proton displacement and electric field (reddish) penetration near the interface. (C) Charged electrode-Nafion interface with inert mobile ions, which are adsorbed at the electrode and which decrease the electric field (reddish) penetration depth.

process cannot be easily obtained, while the surface sites also significantly impact the reversible dissolution potentials. ^{20,54}

Iridium ions can show a variety of oxidation states, the most common are +3, +4, +5, and +6, which are also reported for operating iridium catalysts. ^{21–23} The intermediate states (+3, +5, and +6) of the iridium lattice-ions during the OER may also dissolve in a similar fashion as the previously stated reaction pathways. Moreover, adsorbed ions and hydroxide species may also be involved in the reaction pathways, as for instance described by the following equation:

$$IrO_2OH + OH_{ads} \rightarrow [IrO_4]^{2-} + 2H^+.$$
 [5]

Hence, the presented reactions are just a few examples of pathways for the iridium dissolution with different combinations of involved OER intermediates, ⁵⁵ protons, and oxygen atoms. To summarize, the iridium dissolution during the OER may proceed with cation or anion products, while the detailed chemical and electrochemical pathways are not clarified yet.

The electrochemical interface.—The electrochemical double layer describes the arrangement of charges at the electrochemical interface. In the following, the double layer of the examined electrolytes (Nafion with pure water and Nafion with acid addition) will be discussed. The classic electrostatic models for the double layer will not be considered here for a quantitative description, as these are reported to be affected by errors. Atomistic models for the electrochemical interface based on molecular dynamics and density functional theory are not capable of resolving the complex ion distribution (*n*-body problem) within the interface at large spatial and temporal scales. Thus, only a qualitative and schematic view on the electrochemical interface is presented here.

Nafion shows a phase separation between the water channels and polymeric backbone as thoroughly characterized by cryo-electron-tomography. Separations are mobile backbone as thoroughly characterized by cryo-electron-tomography. Separations are mobile backbone as thoroughly characterized by cryo-electron-tomography. Separations are mobile backbone as thoroughly characterized by cryo-electron-tomography. Separations are mobile backbone as the characterized by cryo-electron-tomography. Separation of Nafion's aqueous phase. Separation of Separation and Separation and Separation and Separation are solutions. From a microscopic perspective, the immobile anionic sulfonic acid groups of Nafion are bound to the rigid polymer matrix, while the protons are mobile. Mobile anions

introduce a further degree of freedom for the ion distribution, dissociation, and transport in the electrolyte and double layer.

Figures 4A-4C show schematic sketches of the anode-Nafion interface with and without mobile anions. The potential with the least surface charge in the double layer is typically defined as potential of zero charge, 60,61 which is here interpreted by similar ion distributions in the electrolytic phase of the electrochemical interface like that in the bulk. Figure 4A aims to display this case, with ion distributions independent of the distance to the electrode. By applying a potential, the ions are rearranged, so that the penetration of the potential into the electrolyte is at least partly shielded. The immobile anions of Nafion cannot significantly move, so that the electric shielding is conducted solely by protons. In Fig. 4B, this case is shown with an applied positive potential, which pushes protons away from the electrode. Yet, the protons are also attracted by the Coulomb force to the covalently bonded anions in the polymer matrix. Figure 4C shows the case of added of mobile anions, where mobile anions accumulate in the double layer due to the positively charged electrode. Consequently, the potential depth of the electric field into the electrolyte decreases, which means that the potential gradient at the electrochemical interface increases.

Hypotheses to explain the effect of inert mobile ions on the iridium dissolution.—In the following, six hypotheses to explain the effect of mobile ions on the iridium dissolution during the OER in Nafion-based electrolytes are presented. Hypotheses I to III are related to bulk properties of electrolytes and ion transport, while hypotheses IV to VI are based on the properties of the electrochemical interface:

I. Without mobile anions, Ir³⁺ may not dissociate in Nafion's aqueous phase. The one-fold charged protons can dissociate into the aqueous phase while they retain similar mobility as that in aqueous solutions.⁴⁴ However, in the case of the three-fold charged iridium cation, the immobile sulfonic acid anions of Nafion may not be able to compensate for the space charge introduced by multivalent cations, while the electroneutrality⁶² in the electrolyte must be retained. As a result, the Ir³⁺ ions may be nearly insoluble in the aqueous phase of Nafion. However, mobile anions alter the microscopic charge arrangement and may locally balance the charge of multi-valent cations, increasing the solubility of Ir³⁺. Similarly, Murawski et al.⁶³ proposed the stabilization of iridium ions in solution by mobile anions.

- II. If anionic iridium complexes [IrO₄]²⁻ dissolve in the aqueous phase of the PEM operated with pure water, the electromigration brings them back to the anode. The mobile protons balance the charge for the iridium anionic complex and thus ensure its mobility within the aqueous phase of Nafion. By adding mobile anions, these and the anionic iridium complexes share the conductance. ^{46,64} The more mobile and inert anions (such as sulfates and perchlorates) accumulate at the anodic interface, ^{46,64} the less likely the formed anionic iridium complexes get in touch with the anode again. Hence, by inert anion accumulation at the anode, the anionic redeposition rate may be reduced, allowing some of the iridium complexes to escape into the feed.
- III. Nafion is an ion exchange material, 65 which adsorbs multivalent cations more strongly than single-valent cations at the anionic sulfonic acid groups. Mobile anions may weaken this electrostatic attraction and thereby increase the Ir3+ mobility. By this increasing mobility the Ir3+ ions can move faster towards the cathode, while the iridium dissolution is no longer hindered by already filled local ion-trapping spots directly at the interface.
- IV. If iridium dissolves as [IrO₄]²⁻ in a PEM electrolyte, it is expected to adsorb in the inner Helmholtz layer of the double layer. Without any other mobile anions, [IrO₄]²⁻ anions may not be able to overcome the electric field gradient in the double layer so that they are trapped at the interface. As a result, [IrO₄]²⁻ anions are redeposited rather than dissolved or at least hinder a further iridium dissolution. If inert mobile anions are also present, they are additionally adsorbed in the inner Helmholtz layer directly at the catalysts. Thus, the electric field trap of the double layer may be overcome by the [IrO₄]²⁻ anions as they are replaced by adsorbed inert mobile anions.
- V. The adsorption of mobile ions in the double layer may decrease the pH value directly at the anodic catalysts. This pH change was reported to lead to higher dissolution rates in liquid electrolytes than in Nafion.⁶⁶
- VI. Mobile anions may affect the phase transition from the solid iridium oxide catalyst to the dissociated form in the liquid phase. The adsorption of mobile anions in the double layer is expected to steepen the electric field gradient in the double layer (see Fig. 4), increasing the driving force for the dissolution process. Moreover, mobile anions may take part in the water intercalation process⁶⁷ during the reaction and the oxygen exchange from the lattice, ¹³ directly affecting the electrocatalytic reaction and the related phase transition for the dissolution. Additionally, anions are reported to alter the adsorption energies during the electrocatalytic OER, ^{50,51} which can change the reaction pathways. Thus, the anions may affect the dynamic recrystallization of the oxide during the OER ^{13,25–28} during the reaction cycles and thereby alter the dissolution mechanism.

The experimental data of Figs. 1 and 2 showed that sulfate ions have a higher impact on the iridium dissolution than perchloric anions. In the following, these findings are related to the plausibility of the presented hypotheses. **Hypothesis** (I) describes that the Ir³⁺ solubility is affected by mobile anions. Metal ions with valences of 3+ or 4+ paired in combination with sulfates are typically less soluble than those paired with perchlorates. In contrast, the solubility of [IrO₄]²⁻ is expected as just slightly impacted by the anions of the acids with respect to their small concentrations of 0.1 M. Hence, this hypothesis cannot explain the different dissolution rates observed with sulfates and perchlorates. In hypothesis (II), the anion complex is redeposited at the anode, while mobile ions electromigrating through the electrolyte interfere in this process. Sulfate ions are just slightly more conductive than perchlorates and with such a small difference it is difficult to explain their drastically different extent on the iridium redeposition. Hypothesis (III) describes the effect of the mobile

anions on the transport of Ir^{3+} in Nafion. However, transport barriers of Ir^{3+} in Nafion without mobile ions are unlikely, as in the PEM fuel cell literature the platinum dissolution at the positive electrode is known to lead to a platinum band $^{68-70}$ inside the PEM. To form such a platinum band, Pt^{3+} ions must be mobile inside the PEM. The mobility of equally charged and similar sized Ir^{3+} ions is expected as similar. Moreover, this hypothesis cannot explain the different effects of sulfates and perchlorates on the iridium dissolution rates.

The hypotheses (IV), (V), and (VI) are all related to the accumulation of mobile anions in the double layer. As the valency of the mobile ions strongly affects the shielding of the electrode potential in the double layer, the double-charged sulfate anions adsorb stronger in the double layer than the single-charged perchlorate anions. Hence, the observed higher iridium dissolution with sulfuric acid addition than that with perchloric acid addition is most likely attributable to the influence of the different anion species on the double layer. Further experimental and computational research is necessary to resolve the impact of the different hypotheses on the iridium dissolution in detail, requiring new approaches and methods that may display topics of future research.

Conclusions

Concluding, the dissolution of the anodic iridium catalyst in a PEM water electrolysis cell was investigated with pure water, 0.1 M sulfuric acid, and 0.1 M perchloric acid feed. Both acids were found to increase the dissolution rate. In the case of sulfuric acid, a drastic dissolution led almost to an almost total loss of the electrically contacted iridium after 22 h of operation at 1 A cm⁻², while the dissolution rate with perchloric acid was estimated as hundredfold smaller. The physicochemical reasons for the effect of the acids' mobile anions on the dissolution were described by six hypotheses. Three of these six hypotheses relate the higher dissolution to electrolyte and transport properties, which however cannot explain the higher dissolution with sulfate in comparison to perchlorate. The three remaining hypotheses depend on the adsorption of the mobile ions in the double layer, where the stronger adsorption of sulfates over perchlorate may explain their different effect on the iridium dissolution. The presented findings build a bridge between the thus far unresolved discrepancy of observed iridium dissolution rates and the intrinsic anion mobility. For long-term stability of in-field operating of PEM water electrolyzers, the accumulation of inert ions in the supply water is conceivable as more harmful for the iridium catalyst than the major but decomposable chloride impurities. Hence, the presented measurements highlight that inert anion pollution of the feed water is critical for the lifetime of iridium-based anode catalysts in PEM water electrolyzers.

Acknowledgments

This work was supported by the German Federal Ministry of Education and Research (BMBF) within the Project DERIEL (03HY122C). We thank Sebastian Lehmann for making Fig. 4.

ORCID

Maximilian Schalenbach https://orcid.org/0000-0002-2040-2483 Andre Karl https://orcid.org/0000-0003-2289-5987

References

- J. H. Russell, L. J. Nuttall, and A. P. Fickett, Am. Chem. Soc. Div. Fuel Chem. Prepr., 18, 24 (1973).
- K. A. Mauritz and R. B. Moore, Chem. Rev., 104, 4535 (2004).
- L. She, G. Zhao, T. Ma, J. Chen, W. Sun, and H. Pan, Adv. Funct. Mater., 32, 1 (2022).
- T. Naito, T. Shinagawa, T. Nishimoto, and K. Takanabe, *Inorg. Chem. Front.*, 8, 2900 (2021).
- H. Wu, Y. Wang, Z. Shi, X. Wang, J. Yang, M. Xiao, J. Ge, W. Xing, and C. Liu, J. Mater. Chem. A, 10, 13170 (2022).
- M. Carmo, D. L. Fritz, J. Mergel, and D. Stolten, *Int. J. Hydrogen Energy*, 38, 4901 (2013).

- 7. S. Cherevko, A. R. Zeradjanin, A. A. Topalov, N. Kulyk, I. Katsounaros, and K. J. J. Mayrhofer, ChemCatChem, 6, 2219 (2014).
- 8. W. Ryden and A. Lawson, Phys. Lett., 26A, 209 (1968)
- 9. J. M. Kahk et al., Phys. Rev. Lett., 112, 1 (2014).
- 10. C. Rozain, E. Mayousse, N. Guillet, and P. Millet, Appl. Catal. B Environ., 182, 153 (2016)
- 11. M. Schalenbach, A. R. Zeradjanin, O. Kasian, S. Cherevko, and K. J. J. Mayrhofer, Int. J. Electrochem. Sci., 13, 1173 (2018).
- 12. A. Lončar, D. Escalera-López, S. Cherevko, and N. Hodnik, Angew. Chemie Int. Ed., 61, e202114437 (2022).
- 13. O. Kasian et al., Energy Environ. Sci., 12, 3548 (2019).
- 14. S. Geiger, O. Kasian, B. R. Shrestha, A. M. Mingers, K. J. J. Mayrhofer, and S. Cherevko, J. Electrochem. Soc., 163, F3132 (2016).
- 15. H. Yu, L. Bonville, J. Jankovic, and R. Maric, Appl. Catal. B Environ., 260, 118194
- 16. C. Minke, M. Suermann, B. Bensmann, and R. Hanke-Rauschenbach, Int. J. Hydrogen Energy, 46, 23581 (2021).
- 17. M. Pourbaix, Atlas of Electrochemical Equilibria in Aqueous Solutions (NACE International Cecelcor Houston) 2nd ed 644 (1974)
- 18. M. Schalenbach, O. Kasian, M. Ledendecker, S. Cherevko, A. Mingers, F. Speck, and K. J. J. Mayrhofer, Electrocatalysis, 9, 153 (2018).
- 19. O. Kasian, J. P. Grote, S. Geiger, S. Cherevko, and K. J. J. Mayrhofer, Angew. Chemie - Int. Ed., 57, 2488 (2018).
- 20. D. Opalka, C. Scheurer, and K. Reuter, ACS Catal., 9, 4944 (2019).
- 21. V. Pfeifer, T. E. Jones, J. J. Velasco Vélez, R. Arrigo, S. Piccinin, M. Hävecker, A. Knop-Gericke, and R. Schlögl, Chem. Sci., 8, 2143 (2017).
- 22. H. G. Sanchez Casalongue, M. L. Ng, S. Kaya, D. Friebel, H. Ogasawara, and A. Nilsson, Angew. Chemie, 126, 7297 (2014).
- 23. T. Weber et al., ACS Catal., 11, 12651 (2021).
- 24. P. E. Pearce et al., Chem. Mater., 31, 5845 (2019).
- 25. P. Jovanovič et al., J. Am. Chem. Soc., 139, 12837 (2017).
- 26. T. Binninger, R. Mohamed, K. Waltar, E. Fabbri, P. Levecque, R. Kötz, and T. J. Schmidt, Sci. Rep., 5, 12167 (2015).
- T. Binninger and M. L. Doublet, *Energy Environ. Sci.*, 15, 2519 (2022).
 V. A. Saveleva, L. Wang, D. Teschner, T. Jones, A. S. Gago, K. A. Friedrich, S. Zafeiratos, R. Schlögl, and E. R. Savinova, J. Phys. Chem. Lett., 9, 3154 (2018).
- 29. D. J. S. Sandbeck, O. Brummel, K. J. J. Mayrhofer, J. Libuda, I. Katsounaros, and S. Cherevko, *ChemPhysChem*, 20, 2997 (2019).
- 30. S. Cherevko et al., *Catal. Today*, **262**, 170 (2016).
- 31. S. Geiger et al., Nat. Catal., 1, 508 (2018).
- 32. M. Milosevic et al., ACS Energy Lett., 8, 2682 (2023).
- 33. M. Ledendecker et al., Nano Res., 12, 2275 (2019).
- 34. M. Bernt, A. Hartig-Weiß, M. F. Tovini, H. A. El-Sayed, C. Schramm, J. Schröter, C. Gebauer, and H. A. Gasteiger, Chemie-Ingenieur-Technik, 92, 31 (2020).
- 35. M. Möckl et al., J. Electrochem. Soc., 169, 064505 (2022).
- 36. F. Hegge et al., ACS Appl. Energy Mater., 3, 8276 (2020).
- 37. M. Clapp, C. M. Zalitis, and M. Ryan, Catal. Today, 420, 114140 (2023).
- 38. S. M. Alia, B. Rasimick, C. Ngo, K. C. Neyerlin, S. S. Kocha, S. Pylypenko, H. Xu, and B. S. Pivovar, J. Electrochem. Soc., 163, F3105 (2016).
- 39. K. Ehelebe, D. Escalera-López, and S. Cherevko, Curr. Opin. Electrochem., 29, 100832 (2021).
- 40. H. Li, S. Zhang, W. Qian, Y. Yu, X. Z. Yuan, H. Wang, M. Jiang, S. Wessel, and T. T. H. Cheng, J. Power Sources, 218, 375 (2012).

- 41. H. Becker, J. Murawski, D. V. Shinde, I. E. L. Stephens, G. Hinds, and G. Smith, Sustain. Energy Fuels, 7, 1565 (2023).
- 42. H. Li, H. Wang, W. Qian, S. Zhang, S. Wessel, T. T. H. Cheng, J. Shen, and S. Wu, I Power Sources 196 6249 (2011)
- 43. E. Kuhnert, O. Kiziltan, V. Hacker, and M. Bodner, ECS Trans., 112, 485 (2023).
- 44. M. Schalenbach, W. Lueke, W. Lehnert, and D. Stolten, *Electrochim. Acta*, 214, 362 (2016)
- 45. C. Wang et al., ChemSusChem, 12, 1576 (2019).
- 46. M. Schalenbach, L. Keller, B. Janotta, A. Bauer, H. Tempel, H. Kungl, M. Bonnet, and R.-A. Eichel, J. Electrochem. Soc., 169, 094510 (2022).
- 47. T. A. Zawodzinski, J. Davey, J. Valerio, and S. Gottesfeld, *Electrochem. Acta*, 40, 297 (1995).
- X. Ren and S. Gottesfeld, J. Electrochem. Soc., 148, A87 (2001).
- 49. M. Carmo, D. L. Fritz, J. Mergel, and D. Stolten, Int. J. Hydrogen Energy, 8, 4901
- 50. S. A. K. Navodye and G. T. K. K. Gunasooriya, J. Phys. Chem. C, 128, 6041 (2024).
- 51. G. A. Kamat, J. A. Z. Zeledón, G. T. K. K. Gunasooriya, S. M. Dull, J. T. Perryman, J. K. Nørskov, M. B. Stevens, and T. F. Jaramillo, Commun. Chem., 5, 1 (2022).
- 52. M. Zlatar, D. Escalera-López, V. Briega-Martos, K. Stojanovski, and S. Cherevko, Electrochim Acta 513 145450 (2025)
- 53. K. Kanaya and S. Okayama, J. Phys. D: Appl. Phys., 5, 43 (1972).
- 54. J. Timmermann et al., Phys. Rev. Lett., 125, 1 (2020).
- 55. L. Giordano, B. Hanb, M. Risch, W. T. Hong, R. R. Rao, K. A. Stoerzinger, and Y. Shao-Horn, Catal. Today, 262, 2 (2015).
- Y. Wang, Y. Song, and Y. Xia, Chem. Soc. Rev., 45, 5925 (2016).
- 57. D. Henderson and D. Boda, Phys. Chem. Chem. Phys., 11, 3822 (2009)
- 58. F. I. Allen, L. R. Comolli, A. Kusoglu, M. A. Modestino, A. M. Minor, and A. Z. Weber, ACS Macro Lett., 4, 1 (2015).
- 59. M. Schalenbach, M. Hoeh, J. Gostick, W. Lueke, and D. Stolten, Phys. Chem. C, 119, 25156 (2015).
- 60. W. Schmickler, Electrochemical Theory: Double Layer (Elsevier Inc., New York) (2014), Reference Module in Chemistry, Molecular Sciences and Chemical Engineering.
- 61. B. B. Damaskin and O. A. Petrii, J. Solid State Electrochem., 15, 1317 (2011).
- 62. B. Janotta, M. Schalenbach, H. Tempel, and R. A. Eichel, *Electrochim. Acta*, 508, 145280 (2024)
- 63. J. Murawski, S. B. Scott, R. Rao, K. Rigg, C. Zalitis, J. Stevens, J. Sharman, G. Hinds, and I. E. L. Stephens, Johnson Matthey Technol. Rev., 68, 147 (2024).
- M. Schalenbach, Y. E. Durmus, H. Tempel, H. Kungl, and R.-A. Eichel, Sci. Rep., 12, 1 (2022).
- 65. H. L. Yeager and A. Steck, Anal. Chem., 51, 862 (1979).
- 66. J. Knöppel, M. Möckl, D. Escalera-López, K. Stojanovski, M. Bierling, T. Böhm, S. Thiele, M. Rzepka, and S. Cherevko, Nat. Commun., 12, 1 (2021).
- 67. S. Lee, Y. J. Lee, G. Lee, and A. Soon, Nat. Commun., 13, 1 (2022).
- 68. T. Jahnke, A. Baricci, C. Rabissi, and A. Casalegno, J. Electrochem. Soc., 167, 149001 (2020)
- 69. L. Kim, C. G. Chung, Y. W. Sung, and J. S. Chung, J. Power Sources, 183, 524 (2008)
- 70. J. Péron, Y. Nedellec, D. J. Jones, and J. Rozière, J. Power Sources, 185, 1209 (2008).
- 71. M. Schalenbach, H. Tempel, and R.-A. Eichel, ChemPhysChem, e202401088 (2025), In Press.